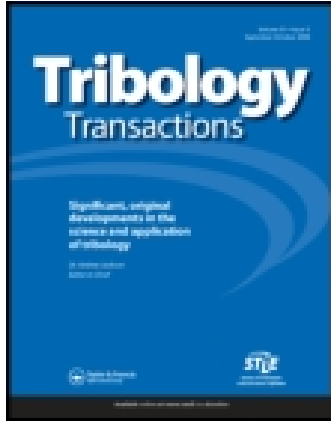


This article was downloaded by: [University of Chicago Library]

On: 08 December 2014, At: 08:23

Publisher: Taylor & Francis

Informa Ltd Registered in England and Wales Registered Number: 1072954 Registered office: Mortimer House, 37-41 Mortimer Street, London W1T 3JH, UK



Tribology Transactions

Publication details, including instructions for authors and subscription information:

<http://www.tandfonline.com/loi/utrb20>

Film Formation in EHL Point Contacts under Zero Entraining Velocity Conditions

F. Guo^a, P. L. Wong^a, P. Yang^b & K. Yagi^c

^a City University of Hong Kong, Department of Manufacturing Engineering and Engineering Management, Kowloon, Hong Kong

^b Qingdao Institute of Architecture and Engineering, Department of Mechanical Engineering, Qingdao, 266033, P. R. China

^c Tokyo Institute of Technology, Department of Mechanical and Aerospace Engineering, Graduate School of Science and Engineering

Published online: 25 Mar 2008.

To cite this article: F. Guo, P. L. Wong, P. Yang & K. Yagi (2002) Film Formation in EHL Point Contacts under Zero Entraining Velocity Conditions, Tribology Transactions, 45:4, 521-530, DOI: [10.1080/10402000208982583](https://doi.org/10.1080/10402000208982583)

To link to this article: <http://dx.doi.org/10.1080/10402000208982583>

PLEASE SCROLL DOWN FOR ARTICLE

Taylor & Francis makes every effort to ensure the accuracy of all the information (the "Content") contained in the publications on our platform. However, Taylor & Francis, our agents, and our licensors make no representations or warranties whatsoever as to the accuracy, completeness, or suitability for any purpose of the Content. Any opinions and views expressed in this publication are the opinions and views of the authors, and are not the views of or endorsed by Taylor & Francis. The accuracy of the Content should not be relied upon and should be independently verified with primary sources of information. Taylor and Francis shall not be liable for any losses, actions, claims, proceedings, demands, costs, expenses, damages, and other liabilities whatsoever or howsoever caused arising directly or indirectly in connection with, in relation to or arising out of the use of the Content.

This article may be used for research, teaching, and private study purposes. Any substantial or systematic reproduction, redistribution, reselling, loan, sub-licensing, systematic supply, or distribution in any form to anyone is expressly forbidden. Terms & Conditions of access and use can be found at <http://www.tandfonline.com/page/terms-and-conditions>

Film Formation in EHL Point Contacts under Zero Entraining Velocity Conditions[©]

F. GUO and P. L. WONG

City University of Hong Kong

Department of Manufacturing Engineering and Engineering Management

Kowloon, Hong Kong

and

P. YANG

Qingdao Institute of Architecture and Engineering

Department of Mechanical Engineering

Qingdao 266033, P. R. China

and

K. YAGI

Tokyo Institute of Technology

Department of Mechanical and Aerospace Engineering

Graduate School of Science and Engineering

The contacts of adjacent balls in a retainerless bearing are subjected to the zero entrainment velocity (ZEV). The existence of an effective elastohydrodynamic lubrication (EHL) film between contacts running under ZEV conditions has long been proven experimentally. However, the classical EHL theory predicts a zero

film thickness under ZEV conditions. Mechanisms, such as the thermal viscosity wedge effect and immobile film theory, have been proposed to tentatively explain the phenomenon. However, detailed numerical results are needed to provide theoretical evidence for such film formations. This paper aims to simulate, based on the viscosity wedge mechanism, the film formation of EHL point contacts under ZEV conditions. Complete numerical solutions have been successfully obtained. The results show that the thermal viscosity wedge induces a concave film profile, instead of a parallel film (Hertzian) as postulated by some previous

Presented at the 57th Annual Meeting
in Houston, Texas
May 19-23, 2002

Final manuscript approved August 23, 2002
Review led by Yeau-Ren Jeng

NOMENCLATURE

a = semiminor axis of Hertzian ellipse, m
 b = semimajor axis of Hertzian ellipse, m
 c, c_1, c_2 = specific heats of lubricants, solids 1 and 2, $J\ kg^{-1}K^{-1}$
 d = dimensionless thickness of the temperature calculation domains of solids 1 and 2
 E' = reduced elastic modulus, Pa
 h = film thickness, m
 \bar{h} = dimensionless film thickness for numerical procedure, hR_x/a^2
 H = dimensionless film thickness for results, $10^5 \times h/R_x$
 \bar{h}_{00} = dimensionless constant
 k, k_1, k_2 = thermal conductivities of lubricants, solids 1 and 2, $W\ m^{-1}K^{-1}$
 k_c = ellipticity parameter, b/a
 p = film pressure, Pa
 p_H = maximum Hertzian pressure, $3w/(2\pi ab)$, Pa
 P = dimensionless film pressure, p/p_H
 R_x, R_y = equivalent radii in the x and y directions, m
 T = temperature, K
 T_0 = ambient temperature, K
 \bar{T} = dimensionless temperature, T/T_0
 u, v = velocities in the x and y directions, $m\ s^{-1}$

u_s = sliding speed, $m\ s^{-1}$
 u_0 = reference speed, $m\ s^{-1}$
 u_1, u_2 = surface velocities of solids 1 and 2 in x direction, $u_1 = u_s/2$, $u_2 = -u_s/2$, $m\ s^{-1}$
 U, V = dimensionless velocities, $U = u/u_0$, $V = v/u_0$
 U_s = dimensionless sliding velocity, $u_s\eta_0/E'R_x$
 w = applied load, N
 W = dimensionless load, $w/E'R_x^2$
 $x, y, z, z_{1,2}$ = coordinates, m
 $X, Y, Z, Z_{1,2}$ = dimensionless coordinates, $X = x/a$, $Y = y/a$, $Z = z/h$, $Z_{1,2} = z_{1,2}/a$
 X_L, X_R, Y_{out} = dimensionless coordinates of the boundaries of the calculation domain,
 α = pressure-viscosity coefficient, Pa^{-1}
 β = thermal viscosity coefficient of lubricants, K^{-1}
 γ = Ry/Rx
 η = viscosity of lubricant, Pa s
 η_0 = ambient viscosity of lubricant, Pa s
 $\bar{\eta}$ = dimensionless viscosity of lubricant, η/η_0
 $\rho, \rho_{1,2}$ = densities of lubricant, solids 1 and 2, $kg\ m^{-3}$
 ρ_0 = ambient density of lubricant, $kg\ m^{-3}$
 $\bar{\rho}$ = dimensionless density of lubricant, ρ/ρ_0

researchers. By the simulation solver developed, the variation of film thickness with loads, oil supply conditions and ellipticity parameters have been investigated. Some unique lubrication behaviors under ZEV conditions are demonstrated. Furthermore, preliminary quantitative comparisons with the latest optical EHL experiments are finished. Both results are in good correlation.

KEY WORDS

Elastohydrodynamic Lubrication; Zero Entrainment Velocity; Viscosity Wedge; Thermal Effect

INTRODUCTION

It has been shown that major problems with the momentum/reaction wheels in spacecraft are associated with the ball bearing retainers or cages, which separate the balls and act as a lubrication reservoir. When the motion of the retainer becomes unstable, problems such as squeal and retainer fractures may occur (Kingsbury and Walker, 1994). In addition, it has been demonstrated that cotton phenolic retainers can actually absorb oil from the bearing instead of supplying the lubricant impregnated before operation (Bertrand, et al., 1995). Hence, it is proposed (Kingsbury, et al., 1978 and 1994) to use retainerless bearings as an alternative and it was demonstrated experimentally that the use of retainerless bearings is a promising option for the future space missions. In a retainerless bearing, the surface velocities of two adjacent balls at the contact point are of the same magnitude but in opposite directions. Thus, no entrainment velocities exist. According to the well founded EHL theory, no film can be built up under zero entrainment (Hamrock and Dowson, 1976, 1977a and 1977b, Cheng, 1965, and Zhu and Wen, 1984). However, several experiments demonstrated that under ZEV conditions, an effective lubricating film between two nonconformal contact surfaces could be built up satisfactorily. To the best of the authors' knowledge, Cameron (1951) was the first to show that under ZEV conditions, disks of line contacts can carry a considerable load. Full oil film was detected between the contact of a steel disk and a bronze disk. However, scuffing occurred almost immediately when a pair of case-hardened steel disks were tested under the same conditions. Cameron ascribed the film built-up to the variation of viscosity across the film originating from the asymmetry of the thermodynamic properties of the bounding surfaces. This film build-up mechanism was termed as "viscosity wedge" later (Cameron, 1958). According to the viscosity wedge effect the necessary difference in the thermodynamic properties could not be satisfied with the steel-steel combination. Hence failure occurred. However, seventeen years later, it was demonstrated (Dyson and Wilson, 1968-69) successfully that with two heavily loaded steel disks with polished surfaces, an effective lubricating film could still be formed. Furthermore, their measurement showed that the film thickness increases with increasing loads. In light of their results, Dyson and Wilson proposed an alternative viscosity wedge occurring in the inlet zone where the surface, moving into the conjunction, is expected to have a lower temperature than the one coming out from the highly pressurized zone. Nevertheless,

these two viscosity wedge effects have not been well accepted, and they are usually ignored in literature reviews and technical books on film formation mechanisms in lubrication. Recently, Shogrin et al. (1998) investigated the oil film formation in ball-ball contacts at ZEV using the capacitance technique. A significant load carrying capacity without surface damage was demonstrated. Their results show that the variation of film thickness does not have a noticeable dependence on speed or load. Shogrin suggested that an immobile boundary film is responsible for the load carrying capacity. More recently, Yagi (2000) succeeded in measuring both the temperature and film profile in steel-sapphire point contact conjunctions under ZEV conditions using an optical test rig. The results revealed for the first time that under ZEV conditions the film profile features a deep dimple within the contact zone instead of a flat plateau as predicted by classical EHL theory. Furthermore, the depth of the dimple increases with increasing load, which is similar to the results of Dyson and Wilson (1968-69).

Obviously, quantitative analysis is crucial to evaluating the roles of the viscosity wedge and immobile boundary film effects, although they both sound reasonable qualitatively. The complete numerical analysis for the film formation of TEHL conjunctions at ZEV is a tough task due to the complexity of the mathematical model and difficulty in numerical method. Some theoretical proofs (Cameron, 1951, and Dyson and Wilson 1968-69) had been provided for the viscosity wedge by using very simple models. Recently, full numerical solutions for line contact TEHL under opposite sliding conditions have been obtained successfully (Yang et al. 2001). Their ZEV numerical results correlate qualitatively well with Dyson and Wilson's experimental results. This paper presents an efficient solver for point contact TEHL under ZEV conditions, and also full numerical solutions for examining the lubrication behavior in retainerless ball bearings. By using numerical simulations, the detailed occurrence of a thermal viscosity wedge within the contact region, which cannot be shown through experiments, is demonstrated. Some intrinsic features of point contact TEHL in ZEV situations, differing from those predicted by classical TEHL, are presented. Furthermore, the preliminary quantitative comparison with the optical EHL experiments (Yagi et al., 2000) has been achieved, showing the significant role of the viscosity wedge.

MATHEMATICAL MODEL

The film formation under ZEV conditions is shown in Fig. 1(a). Two surfaces of solids 1 and 2 run with equal speeds but in opposite directions. The sliding speed u_s is defined as $u_s = u_1 - u_2$ here. The coordinate assignment for modeling the TEHL at ZEV is also shown in Fig. 1. With consideration of the variation of viscosity with temperature across the film, the modified Reynolds equation under ZEV conditions can be derived as an extension of Yang and Wen's work (1990). Its dimensionless form is as follows:

$$\frac{\partial}{\partial X}(\epsilon \frac{\partial P}{\partial X}) + \frac{\partial}{\partial Y}(\epsilon \frac{\partial P}{\partial Y}) = U_s \frac{\partial}{\partial X}(\bar{\Phi} \bar{h}) \quad [1]$$

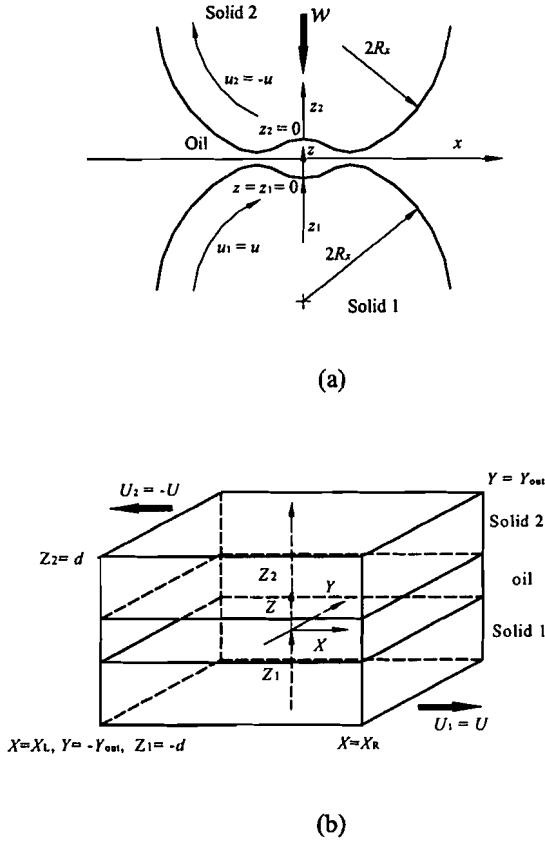


Fig. 1—EHL under ZEV conditions.
 (a) film formation of a ZEV contact
 (b) dimensionless computation domain

where

$$\varepsilon = \overline{(\rho/\eta)_e} \bar{h}^3 / \lambda, \quad \lambda = 6E'R_x^3/a^3p_H,$$

$$\overline{(\rho/\eta)_e} = 12(\bar{\eta}_e \bar{\rho}'_e / \bar{\eta}'_e - \bar{\rho}''_e), \quad 1/\bar{\eta}_e = \int_0^1 1/\bar{\eta} dZ,$$

$$1/\bar{\eta}'_e = \int_0^1 Z/\bar{\eta} dZ, \quad \bar{\rho}'_e = \int_0^1 \bar{\rho} \int_0^z 1/\bar{\eta} dZ' dZ,$$

$$\bar{\rho}''_e = \int_0^1 \bar{\rho} \int_0^z Z'/\bar{\eta} dZ' dZ,$$

$$\bar{\Phi} = \bar{\eta}_e \int_0^1 \bar{\rho} (\int_z^1 1/\bar{\eta} dZ' - \int_0^z 1/\bar{\eta} dZ') dZ.$$

Usually in EHL calculation, a rectangular computation domain is preferred to facilitate programming. Under EHL conditions when the oil gets into the divergent outlet space, the film pressure drops abruptly and some dissolved gases come out of the oil, which has been observed in optical experiments and termed as cavitation. In the cavitated zone the oil film pressure maintains about its saturation vapor pressure. Hence in the whole computation domain, only the film formation behavior out of the cavitation region is governed by the Reynolds Eq. [1]. The oil film pressure in the cavitated area remains at saturation pressure level. The border L between the cavitation region Σ_c and the Reynolds-equation-governed region Σ_R can be determined by the film rupture points. The ambient pressure and the saturation vapor pressure of

oils can be neglected compared to the high pressure generated in the EHL contact. Hence in the whole computation domain, the governing equation is

$$\begin{cases} \frac{\partial}{\partial X} (\varepsilon \frac{\partial P}{\partial X}) + \frac{\partial}{\partial Y} (\varepsilon \frac{\partial P}{\partial Y}) = U_s \frac{\partial}{\partial X} (\bar{\Phi} \bar{h}) & (X, Y) \in \Sigma_R \\ P = 0 & (X, Y) \in \Sigma_c \end{cases} \quad [2]$$

Considering the mass flow continuity, along the boundary L the pressure gradient should also be zero. For Reynolds equation, the boundary conditions imposed can be written as

$$\begin{cases} P = 0, & (X, Y) \in \partial \Sigma_R - L \\ P = \partial P / \partial X = \partial P / \partial Y = 0 & (X, Y) \in L \end{cases} \quad [3]$$

The second relation in Eq. [3] is also called Reynolds cavitation boundary condition (Hamrock, 1994). In numerical computation, boundary L is floating and depends on the operating conditions. The film rupture points are determined through detecting the value of the computed pressure. Boundary L is adjusted during the pressure iteration process, which can make the solver complicated to some degree. Fortunately, Christopherson (Christopherson, 1941) demonstrates that the Reynolds cavitation boundary condition can be implemented alternatively in such a way that at the computation domain boundary the condition of $P = 0$ is imposed; within the computation domain, whenever the calculated pressure of a point is negative, it is set to zero. This treatment can be expressed as,

$$\begin{cases} P(X_L, Y) = P(X_R, Y) = P(X, \pm Y_{out}) = 0 \\ P(X, Y) \geq 0 (X_L < X < X_R, -Y_{out} < Y < Y_{out}) \end{cases} \quad [4]$$

Ignoring the heat conduction in the X and Y directions, the dimensionless energy equation of the oil film can be written as:

$$\begin{aligned} CTS_1 \left(\frac{\partial \bar{T}}{\partial X} \bar{\rho} U + \frac{\partial \bar{T}}{\partial Y} \bar{\rho} V - \frac{\bar{q}}{\bar{h}} \frac{\partial \bar{T}}{\partial Z} \right) &= \frac{1}{\bar{h}^2} \frac{\partial^2 \bar{T}}{\partial Z^2} \\ + CTS_2 \left(U \frac{\partial P}{\partial X} + V \frac{\partial P}{\partial Y} \right) \frac{\bar{T}}{\bar{\rho}} \\ + CTS_3 \frac{\bar{\eta}}{\bar{h}^2} \left[\left(\frac{\partial U}{\partial Z} \right)^2 + \left(\frac{\partial V}{\partial Z} \right)^2 \right] \end{aligned} \quad [5]$$

where $CTS_1 = c\rho_0 u_0 a^3 / R_x^2 k$, $CTS_2 = 0.00065 u_0 \rho_H a^3 / R_x^2 k$, $CTS_3 = u_0^2 \eta_0 / k T_0$, $\bar{q} = \frac{\partial}{\partial X} (\bar{h} \int_0^Z \bar{\rho} U dZ') + \frac{\partial}{\partial Y} (\bar{h} \int_0^Z \bar{\rho} V dZ')$.

The dimensionless energy equations for bounding solids 1 and 2 are given by

$$\frac{c_i \rho_i u_i a}{k_i} \frac{\partial \bar{T}}{\partial X} = \frac{\partial^2 \bar{T}}{\partial Z_i^2} \quad (i = 1, 2) \quad [6]$$

Equations [5] and [6] can be coupled by the continuity of temperature and heat flux at the solid-liquid interfaces, i. e.,

$$\begin{aligned} \bar{T}|_{Z=0} = \bar{T}|_{Z_1=0}, \bar{T}|_{Z=1} = \bar{T}|_{Z_2=0}, \\ \frac{kR_x}{k_1a} \frac{1}{\bar{h}} \frac{\partial \bar{T}}{\partial Z} \Big|_{Z=0} = \frac{\partial \bar{T}}{\partial Z_1} \Big|_{Z_1=0}, \\ \frac{kR_x}{k_2a} \frac{1}{\bar{h}} \frac{\partial \bar{T}}{\partial Z} \Big|_{Z=1} = \frac{\partial \bar{T}}{\partial Z_2} \Big|_{Z_2=0} \end{aligned} \quad [7]$$

It should be noted that if heat conduction in the X and Y directions is considered, the energy equations are of elliptic type. According to the partial differential equation theory, for the elliptic equations to be a well-posed problem, temperature at every point of the boundary of the 3-D computation domain has to be known. However it is difficult to determine the temperature at the downstream boundary of the film or solids in a finite computation domain. In the present cases, the heat conduction in the X and Y directions is much less than the heat conduction in the Z direction and can be ignored (Gohar, 2001), then the energy equations are changed to be of parabolic type. Hence, the temperature value in the downstream boundaries, at which lubricants or solids are leaving the EHL region, is no longer needed for the boundary and initial conditions of the parabolic energy equations (Carnahan, et al., 1969). Similar treatment can be found in boundary layer problems (Schlichting, 1978).

Along Z_1 or Z_2 direction, the boundary conditions ambient temperature are imposed on the points at the outside boundaries of the bounding solids and expressed as

$$\bar{T}(X, Y, Z_1)|_{Z_1=-d} = 1, \bar{T}(X, Y, Z_2)|_{Z_2=d} = 1 \quad [8]$$

According to their moving directions, the initial conditions of the bounding solids 1 and 2 are given at the "initial upstream level" and read

$$\bar{T}(X, Y, Z_1)|_{X=X_L} = 1, \bar{T}(X, Y, Z_2)|_{X=X_R} = 1 \quad [9]$$

However, the initial conditions of the film are not so direct as those of the solids. For example, in the X direction, at the boundary of $X = X_L$ some points have positive velocities indicating the lubricant entering the contact region. These points are at the "initial upstream level" and their temperatures are set to $\bar{T} = 1$ as initial conditions. Those points of negative velocities represent the lubricant leaving the conjunction, are at the "late downstream level" and hence no initial conditions are given. The temperature values of the negative-velocity points depend on the initial conditions imposed on their initial upstream points, some of these upstream points are at $X = X_R$; some are the stagnation points in the X direction within the film, which are floating during the numerical iteration process and can be regarded as implicit initial conditions. At boundaries of $Y = \pm Y_{\text{out}}$, all the points are at late downstream level and no initial conditions can be set. The temperatures of the points at $Y = \pm Y_{\text{out}}$ are also determined by their initial upstream points which are all at $Y = 0$ and stagnant in the Y direction since the present problem is symmetrical about $Y = 0$. Hence in the Y direction, the initial conditions are implicit and floating during the iteration. So the initial conditions of Eq. [5] can be written as

$$\begin{cases} \bar{T}(X_L, Y, Z) = 1 & \text{if } U(X_L, Y, Z) \geq 0 \\ \bar{T}(X_R, Y, Z) = 1 & \text{if } U(X_R, Y, Z) \leq 0 \end{cases} \quad [10]$$

The film thickness in dimensionless form is given as:

$$\bar{h}(X, Y) = \bar{h}_{00} + \frac{X^2}{2} + \frac{Y^2}{2\gamma} + \frac{2\varphi}{\pi^2} \iint \frac{P(X', Y') dX' dY'}{\sqrt{(X-X')^2 + (Y-Y')^2}} \quad [11]$$

where $\varphi = \pi(1 + \gamma)/(4F_2\gamma)$, $F_2 = \int_0^{\frac{\pi}{2}} [1 - (1 - k_e^{-2}) \sin^2 \zeta]^{\frac{1}{2}} d\zeta$.

The dimensionless form of the load balanced equation reads:

$$\iint P dX dY = \frac{2}{3} \pi k_e \quad [12]$$

The dimensionless form of Roelands viscosity-pressure-temperature relationship for lubricants (Roelands et al., 1963) is employed as:

$$\bar{\eta} = \exp\{A_1[(1 + A_2P)^{Z_0}(A_3\bar{T} - A_4)^{-S_0} - 1]\} \quad [13]$$

where $A_1 = \ln(\eta_0) + 9.67$, $A_2 = 5.1 \times 10^{-9} p_H$, $A_3 = T_0/(T_0 - 138)$, $A_4 = 138/(T_0 - 138)$, $Z_0 = \alpha p_H / A_1 A_2$, and $S_0 = \beta (T_0 - 138)/[\ln(\eta_0) + 9.67]$.

The lubricant density is given by Dowson-Higginson relation (Dowson and Higginson, 1966) as:

$$\bar{\rho} = 1 + \frac{0.6 \times 10^{-9} p_H P}{1 + 1.7 \times 10^{-9} p_H P} - 0.00065 T_0 (\bar{T} - 1) \quad [14]$$

NUMERICAL SCHEME

The numerical solution of the governing equations described above is carried out by the pressure-temperature iteration between the Reynolds Eq. [1] and the energy Eqs. [5] and [6] with their boundary conditions.

The Reynolds equation is solved by a multigrid technique similar to that used by Venner and Lubrecht (2000). The elastic deformation is evaluated by the multilevel multi-integration (MLMI) method (Brandt and Lubrecht, 1988). Under the ZEV conditions, the relaxation of the Reynolds equation in each level is performed in two opposite directions alternately, i.e. one direction is from X_L to X_R and the other X_R to X_L . The solver for the energy equations is the same as that developed by Guo, et al. (2001) except that more dense grids are used. In the temperature solver, the unconditionally stable implicit discretization form and related numerical scheme of parabolic partial differential equation are applied to the energy equations. For example, in the X direction within the film, for points of $U \geq 0$, the first-order backward difference is used to approximate convection term $(\partial \bar{T} / \partial X)_{i,j,k}$, i.e., $(\partial \bar{T} / \partial X)_{i,j,k} = (\bar{T}_{i,j,k} - \bar{T}_{i-1,j,k}) / \Delta X$; for points of $U < 0$, the first-order forward difference is applied, i.e. $(\partial \bar{T} / \partial X)_{i,j,k} = (\bar{T}_{i+1,j,k} - \bar{T}_{i,j,k}) / \Delta X$. As to the conduction term, the second-order central difference is used.

In the present solver, the computation domain is given by $X_L = -3.0$, $X_R = 3.0$ (except for the starvation cases), $Y_{\text{out}} = 1.5k_e + 0.5$, $d = 3.15$. The value of d , the depth of the heat conduction parts, is large enough that the temperature gradient is zero at $Z_1 = -d$ and $Z_2 = d$. In the multigrid solver for the Reynolds equation, equidis-

Density of steel, kg m^{-3}	7.85×10^3
Specific heat of steel, $\text{J kg}^{-1} \text{K}^{-1}$	460
Thermal conductivity of steel, $\text{W m}^{-1} \text{K}^{-1}$	47
Density of NYE-182, kg m^{-3}	0.83×10^3
Specific heat of NYE-182, $\text{K kg}^{-1} \text{K}^{-1}$	2000
Thermal conductivity of NYE-182, $\text{W m}^{-1} \text{K}^{-1}$	0.14
Pressure-viscosity coefficient of NYE-182, Pa^{-1}	2.05×10^{-8}
Ambient viscosity of NYE-182, Pa s	0.105
Thermal viscosity coefficient of NYE-182, K^{-1}	0.039
Reduced elastic modulus of steel-steel contacts, Pa	2.28×10^{11}
Reduced radius of the contact in the x direction, m	0.0127
Ambient temperature, K	295

tant 257 nodes in the X direction and 193 nodes in the Y direction in the finest level are employed and also used for the solution of the three-dimensional energy equations. Across the film, 20 equidistant nodes are used. In each bounding solid, 12 non-equidistant nodes along the Z_1 or Z_2 directions are adopted. The mesh size is very small at the interface, and then increases in a geometrical series to facilitate programming. The convergence criterion are adopted as follows:

$$\frac{\sum |P_{i,j}^{new} - P_{i,j}^{old}|}{\sum P_{i,j}^{new}} < 0.0005$$

$$\frac{\sum |T_{i,j,k}^{new} - T_{i,j,k}^{old}|}{\sum T_{i,j,k}^{new}} < 0.0001$$

$$\frac{|\sum S_{i,j} P_{i,j}^{new} - 2\pi k_e/3|}{2\pi k_e/3} < 0.001$$

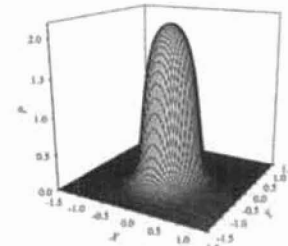
where $S_{i,j}$ is the weight factor of the Simpson's quadrature.

RESULTS AND DISCUSSION

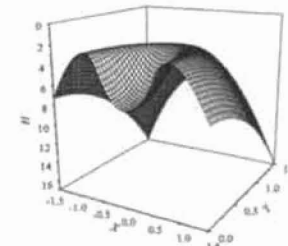
Steel-Steel Contacts under ZEV Conditions

The oil employed for steel-steel contacts is NYE-182 of PAO origin. PAOs are usually used in gyro bearings in spacecraft. The properties of the conjunction and the oil and other input parameters are tabulated in Table 1. The reference speed is $u_0 = 0.547$ m/s.

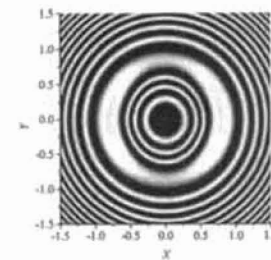
In EHL studies, some actions for film generation have been well understood (Hamrock, 1994), for example, geometrical wedge with entrainment, density wedge and stretch effect, etc.. However, under ZEV conditions, the best known geometrical wedge action accompanied by entrainment is out of function. The behaviors of EHL under the effect of viscosity wedge are believed to have some differences from those by geometrical wedge. Figure 2 illustrates a typical TEHL numerical solution of steel-steel contacts at ZEV under conditions of load $W = 5.96 \times 10^{-7}$ ($p_H = 0.7$ GPa), sliding speed $U_S = 14.62 \times 10^{-11}$ ($u_S = 4.0$ m/s) and k_e



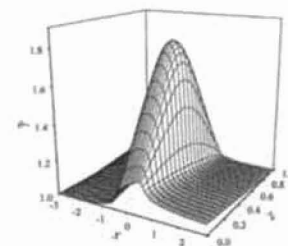
(a)



(b)



(c)



(d)

Fig. 2 Numerical solution of TEHL at ZEV, $W = 5.96 \times 10^{-7}$ ($p_H = 0.7$ GPa), $U_S = 14.62 \times 10^{-11}$ ($u_S = 4.0$ m/s) and $k_e = 1$.

- (a) pressure distribution
- (b) film thickness distribution
- (c) pseudo-interference pattern
- (d) temperature distribution across film at $Y = 0$

= 1. It is obvious that in the ZEV situation the calculated pressure and film thickness distributions are quite different from those predicted in conventional EHL cases. The central pressure ($P_{cen} = 2.135$) is much higher than the maximum Hertzian pressure. Hence, the induced elastic deformation displays a conical depression (dimple) in the central region rather than a flat plateau. The pseudo-interference pattern, with the calculated film thickness data, shows no side lobes, which is a unique feature in the traditional optical EHL.

TABLE 2—EFFECT OF OIL SUPPLY ON THE RESULTS OF EHL AT ZEV

X_L	X_R	H_{cen}	H_{min}	P_{cen}	\bar{T}_{max}	f	X_L	X_R	H_{cen}	H_{min}	P_{cen}	\bar{T}_{max}	f
-3.0	3.	4.302	1.910	3.127	1.703	0.063	-1.1	1.1	4.448	1.865	3.243	1.723	0.061
-4.5	1.5	4.351	1.937	3.157	1.707	0.062	-1.0	1.0	4.456	1.827	3.275	1.728	0.058
-1.5	1.5	4.369	1.876	3.168	1.711	0.060	-0.9	0.9	4.460	1.766	3.311	1.735	0.058
-1.25	1.25	4.428	1.893	3.210	1.717	0.060	-0.8	0.8	4.354	1.560	3.580	1.751	0.059

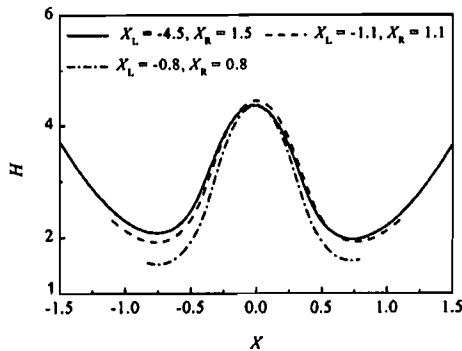


Fig. 3—Film profile under different oil supply conditions, $W = 1.11 \times 10^{-7}$, $U_S = 14.62 \times 10^{-11}$ and $k_e = 1$.

Since the early 1970s, the influence of lubricant supply on EHL behaviors has received serious consideration because of some machine element failures due to lubrication starvation. The theoretical investigation can be achieved by adopting different starting points for the inlet boundary. The work by Hamrock and Dowson (Hamrock and Dowson, 1977b, and Hamrock, 1994) shows that usually numerical starvation can be demonstrated clearly when the dimensionless inlet boundary coordinate is reduced to $-1.5 \sim -2$ (according to the present coordinate system). The starvation can lead to a decrease of oil film thickness by about 50% compared with fully flooded situation. Under conditions of ZEV, a series of calculations have been carried out in this paper to examine the influence of limited oil supply on pressure and film formation. The results are quite different from those in the classical EHL theory. Table 2 lists some of the results, showing variations of the central film thickness H_{cen} , the minimum film thickness H_{min} , the central pressure P_{cen} , the maximum temperature in the film \bar{T}_{max} and friction coefficient f with different calculation boundaries. It can be seen that only when the numerical oil supply boundary (X_L, X_R) is within $(-1, 1)$, the starvation effect can be observed. There is an obvious decrease of the minimum film thickness and an increase of the central pressure. When (X_L, X_R) ranges from $(-3.0, 3.0)$ to $(-1.0, 1.0)$, no noticeable variation of oil film can be observed and the oil supply is still fully flooded. It can be seen that for different dominating actions of film formation, the fully flooded-starved boundary (Hamrock, 1994) at which the minimum film thickness first starts to change when the computation boundary is reduced, is quite different. According to present results, at ZEV the EHL conjunction has a much less fully flood-

ed-starved boundary. Figure 3 gives the pressure and film profiles at ($X_L = -4.5, X_R = 3.0$), ($X_L = -1.1, X_R = 1.1$) and ($X_L = -0.8, X_R = 0.8$) for $W = 1.11 \times 10^{-7}$, $U_S = 14.62 \times 10^{-11}$ and $k_e = 1$. The numerical results show that under conditions of ZEV, full oil film can be sustained with a much smaller supply of oil than that in ordinary EHL cases. Jones, et al. (1997) studied experimentally the performance of retainerless bearings and found that in spite of the average flow rate of 0.1 mg/hour provided by an oozing flow lubricator, the bearing had demonstrated good operation for 440 days. Yagi, et al. (2001) also confirmed experimentally that the full film can be formed in a classical starvation situation.

Based on the conservation of mass, the net mass flow \bar{m}_{net} which is the resultant of the Couette and Poiseuille flows must be constant at different positions except for the cavitation area. For example, in steady state line contact EHL problems, the dimensionless net mass flow rate as a constant can be calculated as:

$$\bar{m}_{net} = \bar{h} \int_0^1 (\bar{\rho}\bar{u})_{\frac{\partial p}{\partial x}=0} dZ \quad [15]$$

where the definition of the parameters are analogous to those in the nomenclature. The dimensionless Couette mass flow is expressed by

$$\bar{m}_{couette} = \bar{h} \int_0^1 \bar{\rho}\bar{u} dZ \quad [16]$$

Hence, a normalized mass flow rate \bar{m}_N , due to the pressure gradient effect, can be defined as

$$\bar{m}_N = (\bar{m}_{net} - \bar{m}_{couette})/\bar{h} \quad [17]$$

Higher values of \bar{m}_N indicate a stronger effect of pressure generation action. When \bar{m}_N is zero, no pressure gradient is induced. For point contact problems discussed here, the Couette mass flow only exists in the X direction. On the central plane of $Y = 0$, side leakage is small compared with that in other locations. Hence Eqs. [15]-[17] can be employed to evaluate qualitatively the pressure generation behaviors under ZEV conditions along the central line of $Y = 0$. One case study is illustrated in Fig. 4. \bar{m}_N has its maximum magnitude within the Hertzian contact region. The thermal viscosity wedge effect is much stronger within the contact region, which differs from the postulation by Dyson and Wilson (1968-69).

Figure 5 shows the temperature and viscosity distributions and the lubricant mass flow profiles across the film at several locations along the X axis to gain more insights into the development of viscosity wedge action. Figure 5(a) is for an upstream position. The top surface comes out from the contact and has a higher temperature. The Poiseuille effect on the total amount of flow is only min-

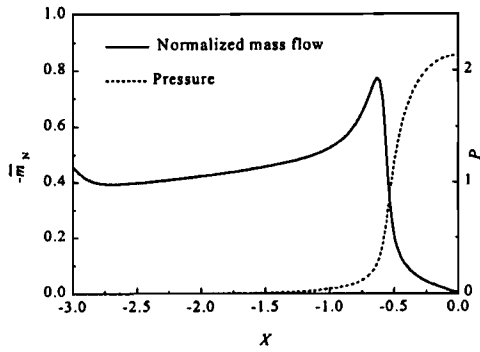


Fig. 4—Normalized mass flow rate and pressure generation under ZEV conditions, $W = 5.96 \times 10^{-7}$, $k_e = 1$, $U_S = 14.62 \times 10^{-11}$.

imal. Considering a position inside the contact area as shown in Fig. 5(c), it can be seen that the temperature of the top surface is still higher than the lower surface, but the maximum temperature occurs inside the oil film. Large Poiseuille flow is generated due to the large increase in pressure. At the central position of the contact, the physical situation is symmetrical about the mid plane, i.e., the temperature and viscosity distributions are mirror images, and the total flow curves are symmetrical above and below the mid flow plane, as shown in Fig. 5(e). The viscosity at the wall surfaces is five orders of the magnitude higher than that at the mid plane. As a result, the flow rate in the mid section of the film is much higher than in the vicinity of the two bounding surfaces.

Based on the above numerical results, it can be seen that the strongest viscosity wedge occurs within the contact region, or the region of pressure generation is smaller than that in the Hertzian contact region. This could be the theoretical support of the smaller fully flooded-starved boundary at ZEV than that in ordinary EHL. Furthermore, for balancing the same external loads, a higher central pressure in a smaller pressure generation region at ZEV can be induced than that in Hertzian contact or classical EHL.

The effect of the ellipticity parameter on the EHL at ZEV is also investigated. In the calculation, with different ellipticity parameters the load is adjusted in such a way that the maximum Hertzian contact pressure can be of the same level, 0.6 GPa. The ellipticity parameter k_e ranges from 1.0 to 8.0, $U_S = 14.62 \times 10^{-11}$. Figure 6 illustrates the variation of the central film thickness, the minimum film thickness and the central pressure with k_e . Similar to the traditional EHL, the central film thickness increases with increasing k_e in that the side leakage effect is of less significance at higher k_e in the central region. Nevertheless, the variation of film shapes is interesting. As shown in Fig. 7(a), when k_e is unity, no side lobes are observed. The minimum film thickness locations are found along the central axis of $Y = 0.0$. When k_e increases, as shown in Figs. 7(b)-(d), distinct side lobes appear and are located around the Y axis, indicating the change of the positions of the minimum film thickness. But according to the classical EHL theory, when k_e increases, the side lobes and the location of the minimum film thickness will get nearer to the X axis.

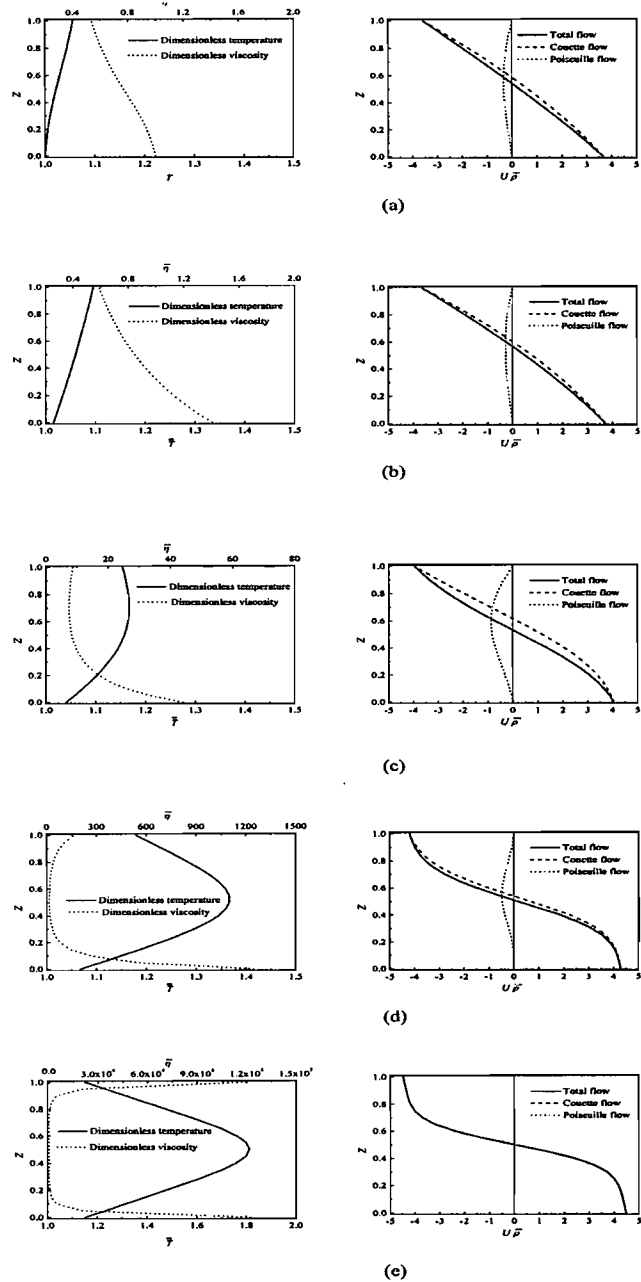


Fig. 5—Numerical results of temperature, viscosity and mass flow across the film at different positions on the plane of $Y = 0$, $W = 5.96 \times 10^{-7}$, $U_S = 7.31 \times 10^{-11}$ and $k_e = 1$

- (a) $X = -2.9$
- (b) $X = -1.0$
- (c) $X = -0.60938$
- (d) $X = -0.53906$
- (e) $X = 0.0$

Steel-Sapphire Contact and Comparison with Experiments

Preliminary quantitative comparison with the experimental results by Yagi, et al.(2001) is performed for further identification of the theoretical viscosity wedge effect. In the analysis, the steel ball is referred to as solid 1, and the sapphire disk as solid 2. For

Density of sapphire, kg m^{-3}	3.98×10^3
Specific heat of sapphire, $\text{J kg}^{-1} \text{K}^{-1}$	577
Thermal conductivity of sapphire, $\text{W m}^{-1} \text{K}^{-1}$	27
Density of P100, kg m^{-3}	0.87×10^3
Specific heat of P100, $\text{J kg}^{-1} \text{K}^{-1}$	2000
Thermal conductivity of P100, $\text{W m}^{-1} \text{K}^{-1}$	0.14
Pressure-viscosity coefficient of P100, Pa^{-1}	2.354×10^{-8}
Ambient viscosity of P100, Pa s	0.214
Thermal viscosity coefficient of P100, K^{-1}	0.0574
Reduced elastic modulus of steel-sapphire contact, Pa	2.90×10^{11}
Ambient temperature, K	295

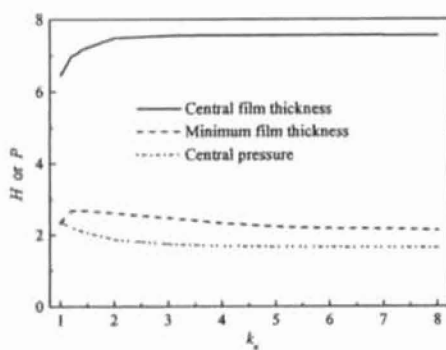
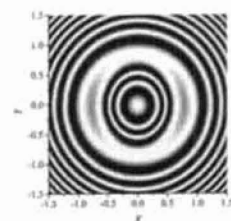


Fig. 6—Effect of ellipticity parameter on EHL at ZEV, $p_H = 0.6 \text{ GPa}$, $U_S = 7.31 \times 10^{-11}$.

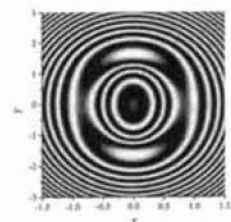
the sake of comparison, in the following section the outputs are given with their original units. Table 3 lists the properties of the conjunctions. Other input parameters are the same as those in Table 1. The thermal viscosity coefficient of lubricant P100 is obtained from the viscosities of P100 at 22°C and 40°C .

Figure 8 shows the theoretical and experimental results under conditions of $u_s = 2.0 \text{ m/s}$, $w = 100.0 \text{ N}$ ($p_H = 1.37 \text{ GPa}$). In obtaining the pseudo-interference pattern, the refractive index of 1.5 and the Lorenz-Lorentz relationship are employed to calculate the optical film thickness. From Fig. 8, in general it can be said that the numerical simulation and the experiment correlate to each other. The average temperature rises within the film obtained by experiment and simulation are of similar profiles. Both show that the temperature rise in the central part is much higher than that in other parts, because the viscous dissipation in the central part is much higher due to the higher viscosity than in other parts. However, the maximum temperature calculated is lower in this case. In Fig. 8(b), both the simulation and the experiment indicate that on the steel ball surface, the temperature in the outlet region is higher than in the inlet region. Calculations also reveal that on the sapphire surface there is similar temperature variation (not presented here). The viscosity wedge originates from such temperature distributions on the bounding surfaces.

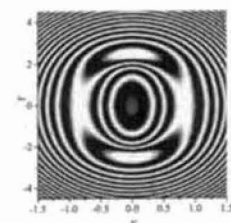
Most interesting is that in the outlet region of the steel surface, the calculated film thickness is always higher than measured. Corresponding Hertzian profile is also plotted as reference. In classical EHL, the film optical interference pattern is of an



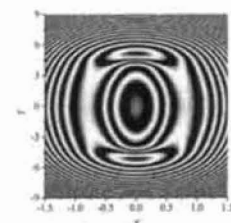
(a)



(b)



(c)



(d)

Fig. 7—Pseudo-interference patterns under different ellipticity parameters, $p_H = 0.6 \text{ GPa}$, $U_S = 7.31 \times 10^{-11}$, wavelength = 500 nm.

- (a) $k_e = 1.0$
- (b) $k_e = 2.0$
- (c) $k_e = 3.0$
- (d) $k_e = 6.0$

approximately circular shape or the film profile is of a Hertzian one when it is out of the contact region, which indicates less distortion. The theoretical results and experiments have had good agreements in this respect (Krupka, et al., 2000). Anyway, it is not true for opposite sliding cases with dimples. In the interference patterns in Fig. 8(e), it can be seen that C_1 and C_3 are distorted in the outlet region of the steel surface. They are stretched along the outlet direction of the steel surface. While in the pseudo-interference patterns, Fig. 8(d), such stretches along the same direction are not observed markedly. To avoid visual delusion, the coordinates of the points in fringes C_1 and C_3 are determined accurately by optical intensity measurement, and C_1 and C_3 are plotted separately as shown in Fig. 8(f) along with two standard circles. In C_1 ,

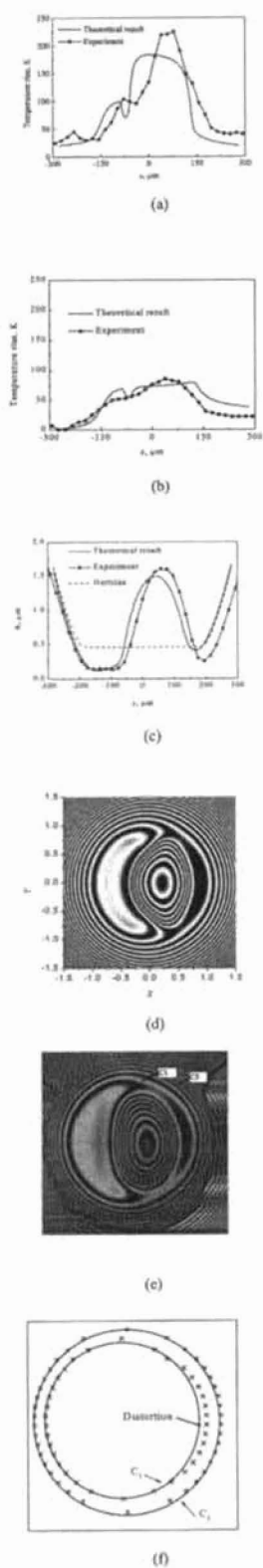


Fig. 8—The theoretical and experiment results, $u_S = 2.0$ m/s, $w = 100.0$ N

($\rho_H = 1.37$ Gpa), $k_e = 1$.

(a) average temperature rise within the film

(b) temperature rise on the steel ball surface

(c) film thickness

(d) pseudo-interference pattern, wavelength = 590 nm

(e) experimental image

(f) local surface distortion

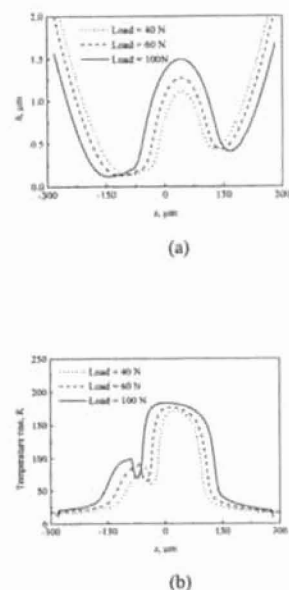


Fig. 9—Effect of load on EHL at ZEV, $u_S = 2.0$ m/s, $k_e = 1.0$.

(a) film thickness

(b) average temperature rise within film

the tangential displacement of the points in the outlet region are pronounced. The obvious shear strain occurring in Fig. 8(f) may originate from the non-uniform shear stress and pressure distributions on the bounding surface. While in classical EHL, the shear displacement on the bounding surfaces is always ignored in the film thickness equation. So in Fig. 8(c), in the outlet region the calculated film thickness is higher. A numerical simulation incorporating the tangential displacement is now under consideration and it is hoped that with tangential displacement in the film thickness equation the distortion of film profile can be addressed clearly. About the interference pattern, it is easily seen that the pattern of the dimple in the simulation is triangular, while that in experiment it is elliptical. Contrary to the situation of steel-steel contacts, the symmetry of the film shape about the Y axis as shown in Figs. 3 and 7 does not exist in sapphire-steel contacts owing to the differences in thermodynamic properties.

Figure 9 illustrates the influence of the loads on the film thickness and pressure distributions. The depth of the dimple increases as the load increases. A similar trend was also recorded by Yagi, et al. (2001). However, the traction behavior shows more difference, as in Fig. 10. Although both curves of friction coefficient versus load have the same tendency, the difference can reach more than 30%. In traditional EHL, the Newtonian model has been criticized for its overestimation of traction. But here the measured friction coefficient is larger than that obtained by the Newtonian model.

CONCLUSION

The numerical simulation is well correlated with the experimental results. It is thus concluded that the film formation in an EHL point contact under ZEV conditions is mainly ascribed to the effect of a thermal viscosity wedge.

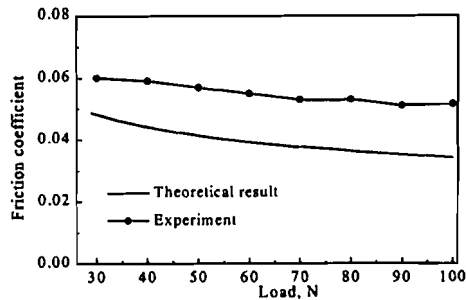


Fig. 10—The friction coefficient obtained by numerical simulation and experiment, $u_s = 2.0$ m/s, $k_e = 1$.

When the two bounding surfaces are of the same material and dimensions, the film profile featuring a large dimple at the central region is symmetrical about the central Y axis.

The film profiles with a deep dimple within the contact region indicate much higher film pressures. This induced high pressure may also be responsible for the lubrication failure except for film breakdown, and should be incorporated into some fatigue analysis of retainerless bearings. The analysis also reveals that the film build-up ability under ZEV conditions can hardly be affected by the oil supply out of the Hertzian contact region. In elliptical contacts, the minimum film thickness occurs around the major axis of the contact ellipse.

ACKNOWLEDGMENTS

The authors would like to express their thanks to Drs. R. C. Lee and E. Y. Lee Charitable Foundation for the award of a research scholarship to F. Guo. Sincere thanks also go to Prof. M. Kaneta of the Kyushu Institute of Technology for his valuable discussion about this subject.

REFERENCES

- (1) Bertrand, E. A., Carre, D. J. and Bauer, R. (1995), "Oil Exchange Between Ball Bearings and Cotton-Phenolic Ball-Bearing Retainers," *Trib. Trans.*, **38**, 2, pp 342-352.
- (2) Brandt, A. and Lubrecht, A. A. (1988), "Multilevel Matrix Multiplication and Fast Solution of Integral Equations," *Jour. of Computational Physics*, **90**, pp 348-370.
- (3) Cameron, A. (1951), "Hydrodynamic Lubrication of Rotating Disks in Pure Sliding. A New Type of Oil Film Formation," *Jour. of Institution of Petroleum*, **37**, pp 471-486.
- (4) Cameron, A. (1958), "The Viscosity Wedge," *ASLE Trans.*, **1**, pp 248-253.
- (5) Carnahan, B., Luther, H. A. and Wilkes, J. O. (1969), *Applied Numerical Methods*, John Wiley & Sons, New York.
- (6) Cheng, H. S. (1965), "A Refined Solution to the Thermal-Elastohydrodynamic Lubrication of Rolling and Sliding Cylinders," *ASLE Trans.*, **8**, pp 397-410.
- (7) Christopherson, D. G. (1941), "A New Mathematical Method for the Solution of Film Lubrication Problems," in *Proc. Inst. Mech. Eng.*, **146**, pp 126-135.
- (8) Dowson, D. and Higginson, G. R., (1966), *Elastohydrodynamic Lubr.*, Pergamon Press, Oxford.
- (9) Dyson, A. and Wilson, A. R. (1968-1969), "Film Thickness in Elastohydrodynamic Lubrication at High Slide/Roll Ratios," in *Proc. Inst. Mech. Eng.*, **183**, 3P, pp 81-97.
- (10) Gohar, R. (2001), *Elastohydrodynamics*, 2nd ed., Imperial College Press, London.
- (11) Guo, F., Yang, P. and Wong, P. L. (2001), "On the Thermal Elastohydrodynamic Lubrication in Opposite Sliding Circular Contacts," *Trib. Int.*, **34**, 7, pp 443-452.
- (12) Hamrock, B. J. and Dowson, D. (1976), "Isothermal Elastohydrodynamic Lubrication of Point Contact: Part 2 – Elliptical Parameter Results," *ASME Jour. of Lubr. Tech.*, **98**, 3, pp 375-383.
- (13) Hamrock, B. J. and Dowson, D. (1977a), "Isothermal Elastohydrodynamic Lubrication of Point Contact: Part 3 – Fully Flooded Results," *ASME Jour. of Lubr. Tech.*, **99**, 2, pp 264-276.
- (14) Hamrock, B. J. and Dowson, D. (1977b), "Isothermal Elastohydrodynamic Lubrication of Point Contact: Part 4 – Starvation Results," *ASME Jour. of Lubr. Tech.*, **99**, 1, pp 15-23.
- (15) Hamrock, B. J., (1994), *Fundamentals of Fluid Film Lubrication*, McGraw-Hill, Inc., New York, pp 465-497.
- (16) Jones, W. R., Shogrin, B. A. and Kingsbury, E. P. (1997), "Long Term Performance of a Retainerless Bearing Cartridge with an Oozing Flow Lubricator for Spacecraft Applications," *NASA TM-107492*.
- (17) Kingsbury, E. P. and Walker, R. (1994), "Motions of an Unstable Retainer in an Instrument Ball Bearing," *ASME Jour. of Trib.*, **116**, pp 202-208.
- (18) Kingsbury, E. P. (1978), "Large Bearing Operation Without Retainer," *Lubr. Eng.*, **35**, 9, pp 517-520.
- (19) Krupka, J., Hartl, M., Poliscuk, R. and Cermak, J., (2000), "Experimental Evaluation of EHD Film Shape and Its Comparison with Numerical Solution," *ASME Jour. of Trib.*, **122**, pp 689-696.
- (20) Roelands, C. J. A., Vulgter, J. C. and Watermann, H., I. (1963), "The Viscosity Temperature Pressure Relationship of Lubrication Oils and Its Correlation with Chemical Constitution," *ASME Jour. of Basic Engineering*, **85**, p 601.
- (21) Schlichting, H. (1978), *Boundary Layer Theory*, 7th ed., McGraw-Hill, New York.
- (22) Shogrin, B. A., Jones, W. R., Kingsbury, E. P., Jansen, M. J. and Prah, J. M. (1998), "Experimental Study of Load Carrying Capacity of Point Contacts at Zero Entrainment Velocity," *NASA TM208650*.
- (23) Venner, C. H. and Lubrecht, A. A. (2000), *Multilevel Methods in Lubrication*, Elsevier Science, Amsterdam, The Netherlands.
- (24) Yagi, K., Kyogoku, K. and Nakahara, T. (2000), "Temperature Measurement of Oil Film and Surface in Point Contact EHL Under High Slip Ratio Condition," in *Proc. of the Int. Trib. Conf. 2000, Nagasaki, Japan*, pp 376-385.
- (25) Yang, P. and Wen, S. (1990), "A Generalized Reynolds Equation for Non-Newtonian Thermal-Elastohydrodynamic Lubrication," *ASME Jour. of Trib.*, **112**, pp 631-636.
- (26) Yang, P., Qu, S., Chang, Q. and Guo, F. (2001), "On the Theory of Thermal-Elastohydrodynamic Lubrication at High Slide-Roll Ratios-Line Contact Solution," *ASME Jour. of Trib.*, **123**, pp 36-41.
- (27) Zhu, D. and Wen, S. Z. (1984), "A Full Solution for the Thermal-Elastohydrodynamic Problem in Elliptical Contacts," *ASME Jour. of Trib.*, **106**, pp 246-254.